Turbulent transition in Rayleigh-Bénard convection with Fluorocarbon

Lucas Méthivier, Romane Braun, Francesca Chillà, Julien Salort

Turbulent transition in Rayleigh-Bénard convection with Fluorocarbon

Lucas Méthivier[1], Romane Braun[1], Francesca Chillà[1] and Julien Salort[1]

[1] *Univ Lyon, ENS de Lyon, CNRS, Laboratoire de Physique, Lyon, France*

Abstract – We present measurements of the global heat-transfer and the velocity field in two Rayleigh-Bénard cells (aspect ratios 1 and 2). We use Fluorinert FC770 as the working fluid, up to a Rayleigh number 2×10^{12}. The velocity field is inferred from sequences of shadowgraph pattern using a Correlation Image Velocimetry (CIV) algorithm. Indeed the large number of plumes, and their small characteristic scale, make it possible to use the shadowgraph pattern produced by the thermal plumes in the same manner as particles in Particle Image Velocimetry (PIV). The method is validated in water against PIV, and yield identical wind velocity estimates. The joint heat-transfer and velocity measurements allow to compute the scaling of the kinetic dissipation rate which features a transition from a laminar $Re^{5/2}$ scaling to a turbulent Re^3 scaling. We propose that the turbulent transition in Rayleigh-Bénard convection is controlled by a threshold Péclet number rather than Rayleigh number, which may explain the apparent discrepancy in the literature regarding the "ultimate" regime of convection.

Introduction.

Turbulent thermal convection is a modern and important problem involved in a lot of practical situations and linked to environmental challenge. Natural flows are indeed difficult to characterize and physicists use often some model systems, such as the Rayleigh-Bénard flows which can mimic a lot of situations and are easy to manage in laboratory. The definition of Rayleigh-Bénard (RB) flow is a fluid layer confined in a cell of characteristics height h on which a difference of temperature $\Delta T = T_{\text{bottom}} - T_{\text{top}}$ is applied to destabilize the flow, so that $T_{\text{bottom}} > T_{\text{top}}$. The non-dimensional parameters characterizing the forcing are the Rayleigh number

$$Ra = \frac{g\alpha\Delta T h^3}{\nu\kappa},\qquad(1)$$

and the Prandtl number

$$Pr = \frac{\nu}{\kappa},\qquad(2)$$

where g is the gravity acceleration, α is the thermal expansion coefficient, ν is the kinematic viscosity and κ the thermal diffusivity, coupled with the aspect ratio $\Gamma = D/h$ where D is the horizontal dimension of the cell.

One of the response parameter is the non-dimensional heat transport, the Nusselt number,

$$Nu = \frac{Qh}{\lambda\Delta T},\qquad(3)$$

where Q is the heat flux injected in the cell, and λ the thermal conductivity. The other important parameter is the Reynolds number

$$Re = \frac{UH}{\nu},\qquad(4)$$

where U is a typical velocity and H a typical scale. As clearly shown in the literature [1,2], the RB flow is largely inhomogeneous and the velocity can change between one place or another of the cell, the definition of H can depend on the place in the cell as well. A point arouse about the scaling laws that can be built as function of the Rayleigh number. To have this kind of discussion, measurements of velocity must be realised in several part of the flow and at different Rayleigh numbers. Two techniques have essentially been used till now: optical measurements such as Laser-Doppler Velocimetry [3–5], Particle Image Velocimetry (PIV) [6–11] or Lagrangian tracking [12,13]; or the measurement of correlation time delay between two probes in a particular point [14–17], recently a measurement of tracking of plumes from shadowgraph pattern have been also introduced [18]. In this letter, we introduce a really cheap and easy to manage method, to get an estimate for the full velocity field. Once this technique is introduced, we will discuss the estimated Reynolds numbers, and their scaling. At the end we will discuss the friction coefficient, and how it relates to the turbulent transition.

Experimental set-up. – We are using in this study two parallelepiped Rayleigh-Bénard convection cells with different aspect ratios. For both cells, the width is 41.5 cm, and the depth is 10.5 cm. The height of the first cell, of aspect ratio $\Gamma = 1$, is 41.5 cm. It is the same cell as previously used [18]. The second is identical but was fitted with smaller glass walls of height 20 cm. Its aspect ratio is $\Gamma = 2$. For both cells, the depth is 4 time smaller than the length so the flow is quasi bi-dimensional.

The cells are made with glass to allow optical measurements with better quality than Polymethyl Methacrylate (PMMA) which yields spurious gradients of optical index. The plates are smooth and made of copper with a thin layer of nickel. The bottom plate is heated with a constant power. The top plate is cooled by a circulation of ethylene-glycol mixture, regulated by a Lauda Variocool chiller. The convection cell is placed inside a PMMA box, thermally regulated at the same temperature as the bulk of the flow. The aim is to reduce the heat losses while keeping the optical access. An additional heat insulation consisting in neoprene foam and a temperature regulated copper thermal screen may be installed around the convection cell. This additional insulation prevents measurements with optical means, but can be used to improve the accuracy of the Nusselt number estimates.

The working fluid is Fluorinert FC770 (produced by 3M), which allows to reach higher Rayleigh numbers than those we had in the same apparatus with deionized water [7]. To compute the non-dimensional parameters, accurate estimates of the physical properties of the fluids are required. While they are well known for deionized water, it is not the case for FC770. Previous studies using FC770, such as [19], used the physical properties at 25 °C provided by the manufacturer. However, a higher working temperature (40 °C) allows to increase the temperature difference, and span a wider range of Rayleigh number. Additionally, the temperature dependence of the physical parameters is useful to estimate the deviation from the Boussinesq approximation. It is therefore difficult to compare the Rayleigh and Nusselt numbers obtained in FC770 with other data from the literature without better estimates of the fluid properties.

Therefore, we got the physical parameters measured by Flucon GmbH, see table 1. The viscosity required to compute the Rayleigh number, is computed from this data as $\nu = \frac{\eta}{\rho}$.

Special care must be taken regarding the thermal conductivity, λ, which is required both for computing the Nusselt number, and for the estimate of the heat diffusivity in the Rayleigh number, $\kappa = \frac{\lambda}{\rho c_p}$. Indeed, most commercial apparatus have not been designed with a fluid such as FC770 which has both low thermal conductivity and low viscosity, and their design produce spurious natural convection. That is why we performed our own measurements of the thermal conductivity using a commercial thermal conductivity analyzer, model "TCi", from C-Therm Tech-

Table 1: Physical properties of FC770 measured by Flucon GmbH. Density ρ, heat capacity c_p, and dynamic viscosity η, for temperatures (T) ranging from -10 °C to 95 °C.

T [°C]	ρ [kg/m^3]	c_p [K/kg/K]	η [Pas]
-10.0	1890.3	932.2	3.0407×10^{-3}
-5.0	1876.6	942.6	2.6885×10^{-3}
0.0	1863.5	959.2	2.3813×10^{-3}
5.0	1849.4	967.0	2.1223×10^{-3}
10.0	1836.7	979.2	1.9154×10^{-3}
15.0	1822.8	991.6	1.7393×10^{-3}
20.0	1809.8	999.5	1.5783×10^{-3}
25.0	1795.9	1007.4	1.4407×10^{-3}
30.0	1782.1	1023.0	1.3364×10^{-3}
35.0	1769.1	1032.7	1.2236×10^{-3}
40.0	1754.9	1048.6	1.1397×10^{-3}
45.0	1741.7	1055.2	1.0585×10^{-3}
50.0	1728.6	1068.7	9.9312×10^{-4}
55.0	1714.4	1071.8	9.2496×10^{-4}
60.0	1700.8	1085.6	8.7276×10^{-4}
65.0	1687.3	1093.8	8.2490×10^{-4}
70.0	1673.8	1102.0	7.7859×10^{-4}
75.0	1660.5	1115.9	7.3521×10^{-4}
80.0	1647.2	1123.7	6.9451×10^{-4}
85.0	1633.0	1135.4	6.6369×10^{-4}
90.0	1619.5	1154.2	6.3422×10^{-4}
95.0	1606.4	1160.8	6.0256×10^{-4}

nologies Ltd, inside a temperature regulated chamber. In this configuration, the measurement is performed on a thin film of liquid, and not with a heated wire. We find the following fit for $\lambda(\theta)$, which we use in the remainder of the paper,

$$\lambda(\theta) = \lambda_0 + (\partial_\theta \lambda)\theta, \qquad (5)$$

where $\lambda_0 = 0.1114$ W/m/K is the thermal conductivity at 0 °C, $\partial_\theta \lambda = 3 \times 10^{-4}$ W/m/K/°C, and θ is the temperature in °C. This value of λ is quite different from the estimate from the manufacturer, $\lambda_{3M} = 0.063$ W/m/K at 25 °C. It is unclear how spurious convection bias the measurement, as it depends on details of the apparatus which are not publicly available. As can be seen in Fig 1, our Nusselt numbers are a bit below the values of the Grossmann-Lohse (GL) model [20]. They would however be much higher than the GL model if λ_{3M} was used instead. It is possible that our measurement with the TCi thermal conductivity analyser slightly overestimates λ. The phenomenological value of λ that would offset our heat-transfer data so that it matches the prediction of the GL model is $\lambda_{GL} = 0.0945$ W/m/K at 25 °C.

The heat transfer measurements are reported in table 2 for both aspect ratio cells without additional insulation, and in table 3 for $\Gamma = 1$ cell with the additional insulation. As can be seen in Figure 1, the scaling law for the Nusselt number obtained with FC770 is close to $Ra^{1/3}$, up to
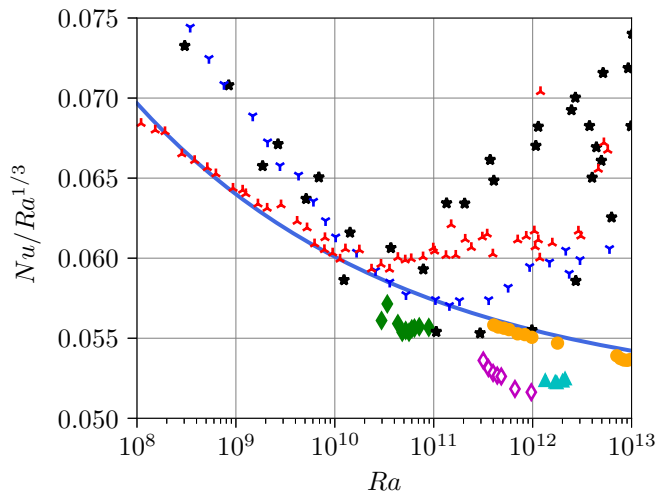
Fig. 1: Heat transfer measurements in FC770 (present work) in the $\Gamma = 2$ cell (green diamonds at 25 °C) and in the $\Gamma = 1$ cell (open magenta diamonds at 25 °C, and cyan triangles at 40 °C). Several high-Rayleigh number heat-transfer measurements are shown for reference: the heat-transfer from Chavanne, et al. [22] ($\Gamma = 1/2$) in black stars, from He, et al. [21] ($\Gamma = 1$) in orange circles, from Niemela, et al. with $\Gamma = 1$ [23] in blue 3-branch stars and $\Gamma = 4$ [24] in red 3-branch stars. Solid lines: estimates from the Grossmann-Lohse model with the updated prefactors [20], for $Pr = 14$.

$Ra = 2 \times 10^{12}$, in fair agreement with the results from He, et al [21], as well as the Grossmann-Lohse model [20]. At this stage, the puzzle remains why it seems to be in disagreement with the data from Chavanne, et al. [22], and from Niemela, et al. [23, 24].

The interpretation proposed by Chavanne, et al. [22] to explain the heat-transfer enhancement that they report, is a laminar turbulent transition of the boundary layer, which yields the inertial regime predicted by Kraichnan [25]. This interpretation was backed by two observations: (i) a transition for the dissipated power from a laminar $\epsilon \sim Re^{5/2}$ regime to a turbulent $\epsilon \sim Re^3$ regime; (ii) a change in the statistics of the temperature fluctuations. The latter was later confirmed with a smaller thermometer [26]. In the following, we focus on velocity measurements, and estimates of the dissipation, to compare the dissipation scaling with the scaling in cells with and without heat-transfer enhancement.

Shadowgraph and velocity measurement. – In this range of Rayleigh numbers, most cells do not allow visualization, and the wind velocity is often estimated from the correlations of local thermometers [16, 17, 22, 27, 28]. In this work, we use optical methods which allow to resolve the velocity field. However, the cost of FC770 as a working fluid makes it unsuitable to particle seeding, as pollution of the working fluid would be very costly. Therefore, we based the measurements on shadowgraph, which is non-invasive and does not pollute the working fluid. The method investigated here may also be useful
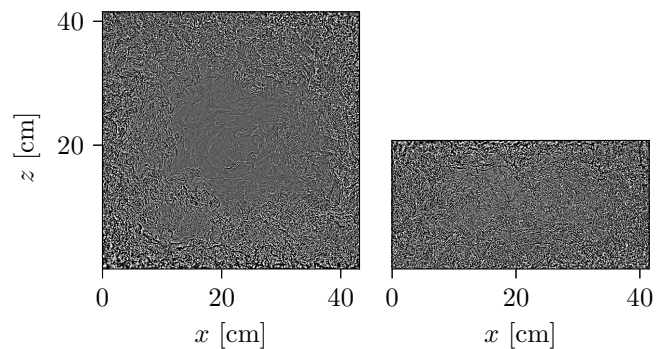

Fig. 2: Shadowgraph images in the Rayleigh-Bénard cell with FC770. Left: Aspect ratio 1 cell at $Ra = 1.3 \times 10^{12}$ (Mean temperature at 40 °C). Right: Aspect ratio 2 cell at $Ra = 8.9 \times 10^{10}$ (Mean temperature at 25 °C).

for other experiments where particle seeding would be impractical, such as fluids at extreme temperatures.

The set-up is similar to the one described in [18], and consists in direct shadowgraphy in diverging light. In this paper, the cell is illuminated by a punctual monochromatic light (M450LP1 LED from ThorLabs). The light source is far enough from the cell, that the light is almost parallel. The shadowgraph pattern is captured on a ground glass diffuser, and recorded with a PCO Pandas camera, with a resolution 2048×2048 pixels. An example of shadowgraph pattern is shown in figure 2. The frame rate of the image sequence varies between 15 Hz at low Ra and 40 Hz at high Ra, to accommodate for the faster plume velocities when Ra is higher. The duration of the sequence is a few turnover times, ranging from 3 minutes and 20 seconds to 8 minutes and 20 seconds.

There are several strategies to infer an estimate of the velocity fields from the shadowgraph images. In a previous work, we investigated a simple method based on space-time diagrams [18]. Because this method tracks the plumes, it allows to infer statistics on the plumes. However, the drawback is that the measurement is averaged over lines. In the present work, we investigate an alternative method which consists in applying to the shadowgraph pattern the same algorithm that we use for Particle Image Velocimetry (PIV), i.e. Correlation Image Velocimetry (CIV) from the CIVx toolbox implemented by Fincham and Delerce [29].

This is possible in this range of Rayleigh numbers, because plumes are relatively small and fill the entire volume, and therefore may act as local pattern for the correlation algorithm similar to the particles in PIV. One important difference between the velocity field obtained in this way compared to the velocity field in PIV is that the light pattern is integrated over the depth of the cell, while particles in PIV are imaged on a light sheet. In our case, however, the flow is quasi bi-dimensional, so the integra-
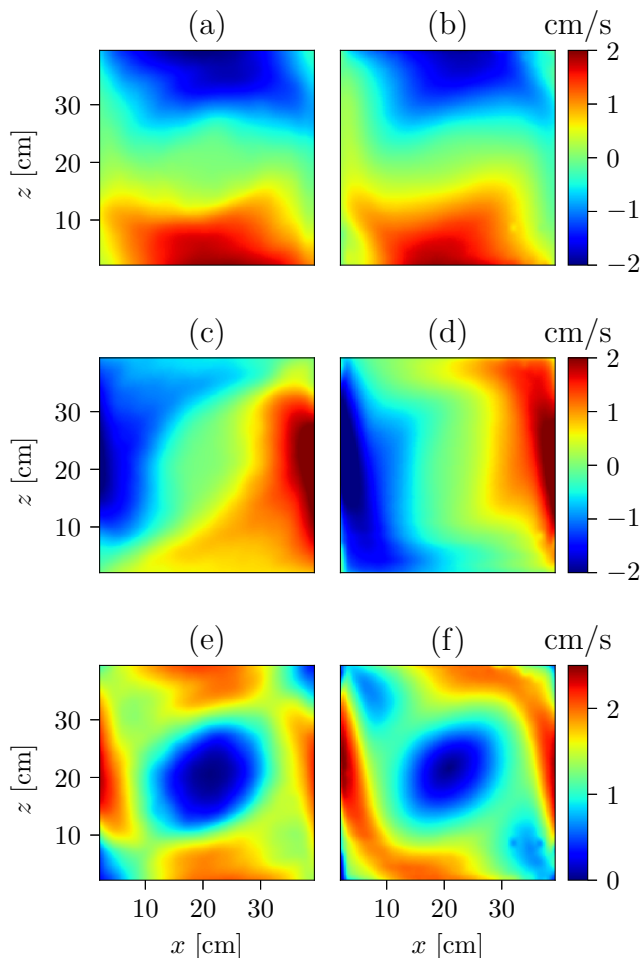
Fig. 3: Right column: velocity field obtained by Liot, et al. [7] using Particle Image Velocimetry (PIV) at $Ra = 6.9 \times 10^{10}$ and $Pr = 4.4$ in water. Left column: velocity field obtained from Correlation Image Velocimetry from the shadowgraph pattern (present work) in the same cell and same Ra and Pr. (a, b) mean horizontal component U, (c, d) mean vertical component V, (e, f) mean velocity magnitude $\sqrt{U^2 + V^2}$.
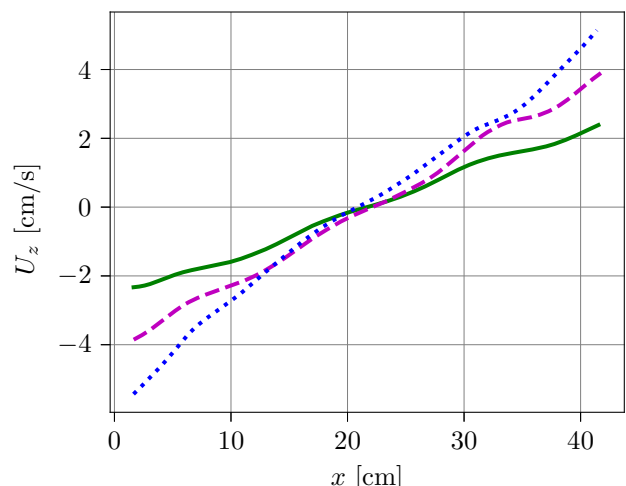

Fig. 4: Velocity profiles at mid-height in the $\Gamma = 1$ cell with FC770 as the working fluid. Solid green line: $Ra = 3.6 \times 10^{11}$, dashed purple line: $Ra = 9.7 \times 10^{11}$, dotted blue line: $Ra = 2.1 \times 10^{12}$.

tion across the depth does not blur excessively the flow field. The CIV box size has to be a bit larger than with PIV, typically 4 mm, for them to hold a usable plume pattern. This means that we cannot resolve the velocity field inside the boundary layers, which are typically one order of magnitude smaller. To validate the method, we applied it to the case of deionized water, for which we could compare against PIV measurement. As can be seen in Figure 3, the average flow pattern is well recovered, except in the corners where both upwelling and downwelling plumes are visible on the shadowgraph sequence, which results in small velocity magnitude in the CIV field. The vertical velocity component near the top and bottom plates also show a qualitative difference. This may be caused by wall flows, such as plume attachment along vertical walls.

Reynolds number and friction coefficient. – There are different kinds of definitions for the Reynolds number in the literature: based on the average velocity, the average turnover time, or the velocity fluctuations. The position of the sensor also varies, which makes it difficult to directly compare the value of the Reynolds numbers. However, Musilovà, et al. have compared estimates based on the sloshing mode frequency, time of flight between thermometers, and average or fluctuating velocities from the Elliptic approximation, and found that all these estimates roughly scale identically [17].

In the following, we choose the height of the cell h, as the length scale H in the estimation of the Reynolds number, and the vertical component of the velocity inside the jet as the typical velocity U. From the mean velocity field, we compute velocity profiles at mid-height, by spatially averaging on a window of height 2 cm. Examples of velocity profiles are shown in Figure 4. We use the point closest to the walls on these velocity profiles to compute the Reynolds number. This is similar to measurements with a fixed sensor. The relative position in the present work is of order 1 % of the cell width, which is comparable to [17, 28]. However, as noted previously [18], the non-dimensional shape of the velocity profile does not seem to change significantly with the Rayleigh number. Therefore, the actual choice for the position of the velocity probe only produce a constant prefactor for the Reynolds number, which however could be as high as 40 % across the published data in the literature. The Reynolds number values are given in Table 2. As can be seen in Figure 5, they are in fair agreement with other Reynolds number data from the literature, with a scaling close to $Ra^{1/2}Pr^{-0.7}$.

We compute the friction coefficient, using the same approach used by [22]. Let us recall that the balance of

Table 2: Reynolds numbers obtained from shadowgraph, and estimated global heat-transfer, in both $\Gamma = 1$ and $\Gamma = 2$ cells, without the copper thermal screen (to allow visualization), using FC770 (Pr between 11 and 14) as working fluids.

Ra	Nu	Pr	Re	Γ
3.4×10^{10}	185.7	14.1	3487	2
3.9×10^{10}	191.1	14.0	3563	2
4.3×10^{10}	197.0	14.1	3829	2
4.8×10^{10}	201.8	14.1	4058	2
5.2×10^{10}	207.6	14.1	4283	2
5.6×10^{10}	212.6	14.1	4539	2
6.0×10^{10}	218.0	14.1	4641	2
6.4×10^{10}	222.7	14.1	4572	2
7.1×10^{10}	231.4	14.1	5124	2
8.9×10^{10}	248.9	14.1	5681	2
3.2×10^{11}	364.7	14.1	12073	1
3.6×10^{11}	382.5	14.1	13909	1
4.0×10^{11}	396.3	14.1	14391	1
4.4×10^{11}	406.6	14.1	14818	1
4.8×10^{11}	415.1	14.0	15904	1
6.6×10^{11}	459.8	14.1	18469	1
9.7×10^{11}	530.4	14.1	22038	1
1.1×10^{12}	557.2	14.1	23338	1
1.3×10^{12}	577.8	12.0	29597	1
1.7×10^{12}	635.3	11.9	32186	1
1.8×10^{12}	627.4	12.5	31321	1
2.0×10^{12}	682.6	11.9	34454	1
2.1×10^{12}	712.3	11.9	36082	1

Table 3: Global heat-transfer measurements in the $\Gamma = 1$ fluorocarbon cell, with the copper thermal screen for more accurate Nusselt number estimates. The Nusselt number is estimated using $Q = Q_{\mathrm{raw}} - Q_{\mathrm{loss}}$, with $Q_{\mathrm{loss}} = -0.7\,\mathrm{W}$ for the 25 °C series, and $Q_{\mathrm{loss}} = 2.5\,\mathrm{W}$ for the 40 °C series.

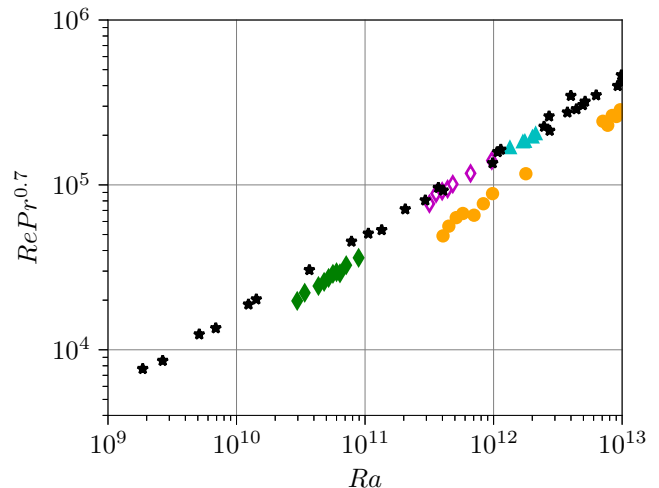| Ra	Nu	Pr	Q_{raw} [W]	ΔT [K]	T_{moy} [°C]
1.2×10^{11}	288.7	14.1	15.7	5.2	25.0
2.3×10^{11}	337.1	14.0	36.0	10.0	25.1
3.0×10^{11}	365.0	14.0	50.7	12.9	25.1
5.0×10^{11}	422.1	14.1	100.7	22.0	25.0
8.6×10^{11}	494.4	14.0	200.7	37.4	25.1
1.0×10^{12}	520.4	14.0	250.9	44.3	25.1
1.6×10^{11}	268.6	11.9	17.4	5.3	40.0
3.5×10^{11}	377.1	11.9	47.5	11.4	40.1
6.2×10^{11}	451.8	11.9	97.5	20.2	40.1
1.5×10^{12}	592.3	11.9	297.4	47.7	40.1
1.8×10^{12}	634.3	11.9	397.4	59.6	40.0
2.2×10^{12}	681.1	11.8	497.5	70.0	41.5

Fig. 5: Reynolds number measurement with FC770 (present work) in the $\Gamma = 2$ cell (green diamonds at 25 °C) and in the $\Gamma = 1$ cell (open magenta diamonds at 25 °C, and cyan triangles at 40 °C). For reference: Reynolds number from Chavanne, et al. [22] (black stars) and from He, et al [28] (orange circles).

kinetic energy yields the following exact relation [1,2],

$$\epsilon = \frac{\nu^3}{h^4}(Nu - 1)RaPr^{-2}, \qquad (6)$$

where ϵ is the kinetic energy dissipation rate. In the developed turbulence limit, one may expect $\epsilon \sim \frac{U^3}{h} \propto Re^3$. The non dimensional ratio,

$$\frac{(Nu - 1)RaPr^{-2}}{Re^3} = \frac{\nu(\mathrm{grad}\,\mathbf{u})^2}{u^3/h}, \qquad (7)$$

is similar to a friction coefficient, and scales like $1/\sqrt{Re}$ at low Reynolds number (viscous limit), and features a plateau in the high Reynolds number limit.

As can be seen in Figure 6, the friction coefficient in the FC770 experiment reaches a plateau at the highest forcing (at Rayleigh numbers larger than 10^{12}). In addition, the value of the plateau is in quantitative agreement with the results from Chavanne, et al. [22] and Niemela, et al. [16,23]. We may note also that the recent data from Musilovà, et al. [17] are also in quantitative agreement with those of Niemela, et al. [23,24]. The data from He, et al. [21,28] also features a plateau, but only at their highest forcing. They are slightly offset compared to the other measurements, but this is of no consequence. Indeed, it may be caused by their slightly lower Reynolds numbers, possibly resulting from the choice of the thermometer positions. In principle, and unlike intrinsic estimates such as the Taylor micro-scale Reynolds number R_λ, all Reynolds number estimates which are based on large scale quantities are defined with a $O(1)$ prefactor. The important point is that they reach the friction *versus Re* plateau, but only at their highest forcing, which is consistent with their transition observed at higher Rayleigh number compared to Chavanne, et al.
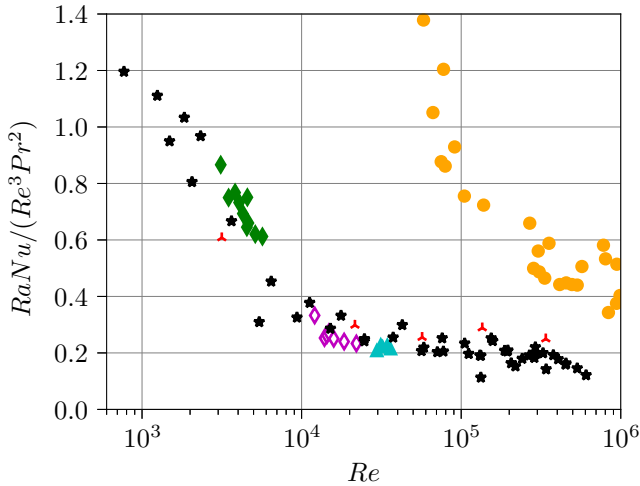
Fig. 6: Friction coefficient *versus* the Reynolds number. Data with the FC770 (present work) in the $\Gamma = 2$ cell (green diamonds at 25 °C) and in the $\Gamma = 1$ cell (open magenta diamonds at 25 °C, and cyan triangles at 40 °C). Black star from Chavanne, et al. [22], red 3-branch stars from Niemela, et al. [16] at aspect ratio 1, orange circles from He, et al. [21, 28].

This seems to indicate that the transition to the "ultimate regime" may be controlled by the Reynolds number rather than the Rayleigh number, as previously suggested by Dubrulle to explain apparent contradictions between measurements in SF_6 (large Re) and in alcohol and water (lower Re) [30]. Although all experiments show a similar Ra versus Re scaling, one must not forget the Pr dependency, as well as possible dependencies on the geometry and flow configurations. Therefore, a threshold on the Reynolds number does not translate into a threshold on the Rayleigh number. Additionally, while the plateau is clearly visible on the present FC770 data, there is no visible heat-transfer enhancement. The reason is that our data lies at the beginning of the friction plateau, and the transition on the Nusselt number is not very sharp.

However, as can be seen in Figure 7, the structure of the large scale circulation (LSC) is identical on the full range of Rayleigh numbers that can be obtained in the cell with FC770. It is also similar to the velocity field obtained in water (see Fig 3) at lower Rayleigh numbers, and in fair agreement with the LSC structure reported by Xia, Sun & Zhou [6] at $Ra = 3.5 \times 10^{10}$. They report however a change from an oval-shaped LSC to the same rectangular-shaped LSC that we observe, at a threshold Rayleigh number of order 10^{10}. The present work indicates that this rectangular-shaped LSC is very robust and remains unchanged from $Ra = 4 \times 10^{10}$ up to $Ra = 2 \times 10^{12}$, in a range where the scaling of the kinetic dissipation rate is compatible with the turbulent regime.

Additionally, as shown in Fig 8, in the high Reynolds number limit, it seems that all Nusselt number data can be fairly well collapsed with the phenomenological scaling,

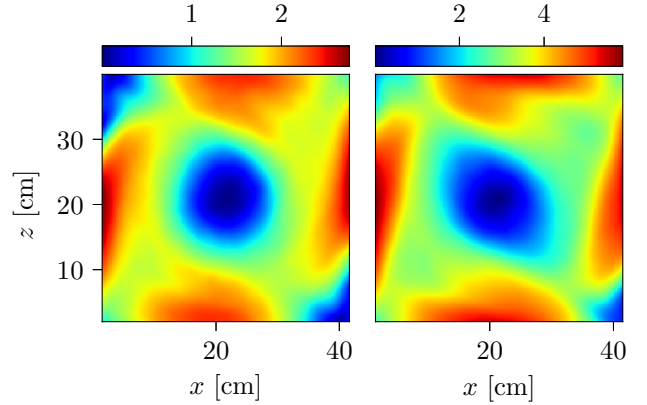$$Nu \sim Re^{0.8}Pr^{0.6}. \tag{8}$$

Fig. 7: Velocity fields in the $\Gamma = 1$ cell with FC770. Left: $Ra = 3.6 \times 10^{11}$ (Mean temperature 25 °C). Right: $Ra = 2.1 \times 10^{12}$ (Mean temperature 40 °C).

More precisely, it seems that the threshold is controlled by the Péclet number, $Pe = RePr$, rather than the Reynolds number, and occurs for a Péclet number of order 10^5. This is somewhat consistent with the analysis of Kraichnan [25].

Conclusion. – We showed that the flow in our cell undergoes a transition to a turbulent regime, where the kinetic energy dissipation scales like Re^3, and the Nusselt number is a universal function of the Reynolds and Prandtl numbers. One possible reason for the apparent discrepancy in the literature is that the transition is controlled by the Péclet number. This might also explain why Roche finds that there is a Ra-dependant transition threshold for the Prandtl number [27]. Indeed, the measurements in SF_6 have a nearly constant Prandtl number of order 0.8, almost ten times lower than the Prandtl number in the high Rayleigh numbers data of Chavanne, et al. As can be seen in Fig 8, they reach similar Péclet number only at their higher forcing.

While the scaling of the Reynolds number with the Rayleigh number is quite robust, the effective Reynolds number may still differ, for a given Ra, in one experiment, compared to another experiment. This discrepancy may be due to the Prandtl number, effects of the geometry, or the actual flow configuration. In addition, it is not possible to define the Reynolds number in a universal way, in a flow which is neither isotropic nor homogeneous. That makes comparison of transition thresholds between experiments intrinsically challenging.

Yet, the intensity of the LSC does not seem to change in the turbulent regime, and the scaling of the Reynolds number is not significantly modified beyond the turbulent transition. This is consistent with the observations of Roche, et al. [27], which showed that the transition in Grenoble did not feature a dramatic change in the LSC either. It is particularly striking that the scaling of the Reynolds number versus Rayleigh number is incredibly consistent across all experiments, whether or not they feature a transition to an enhanced heat transfer regime.
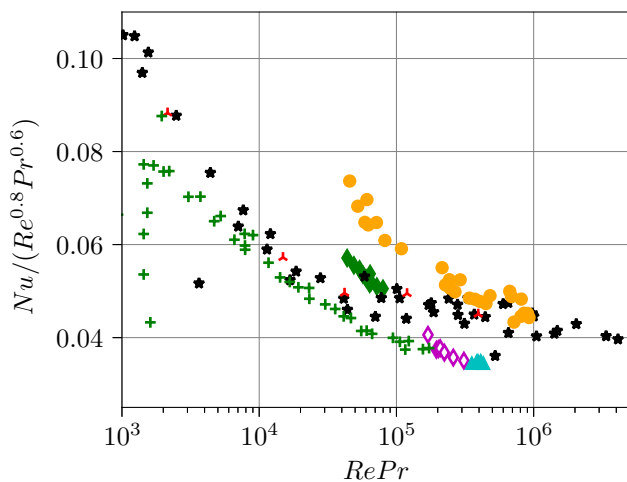
Fig. 8: Compensated Nusselt number as a function of the Péclet number, $Pe = RePr$. When the data gets to a plateau, the scaling is $Nu \sim Re^{0.8}Pr^{0.6}$. The symbols are identical to previous figures, with the addition of the data from Wu Ph.D. thesis [31] (green crosses).

One possible mechanism is that the transition is triggered by the fluctuations, or boundary eddies, as suggested by Roche [32]. It is likely that the velocity fluctuations scale similarly to the average velocity, at least up to the turbulent transition, hence why Re based on the LSC intensity still acts as a good parameter. Remarkably, in the case of roughness-facilitated transitions Liot et al. observed at high Re that the intensity of the LSC was not changed above and below the transition to the enhanced heat transfer regime, but that the intensity of velocity fluctuations and their statistical features, were indeed significantly enhanced [7]. At smaller Re however, the roughness-triggered transition does not necessarily yield higher bulk velocity fluctuations [33], and might therefore be different in nature [34]. It would be useful to further study the velocity fluctuations, and the small scale structures below and above the turbulent transition.

* * *

REFERENCES

[1] Ahlers G, Grossmann S and Lohse D 2009 *Rev. Mod. Phys.* **81** 503

[2] Chillà F and Schumacher J 2012 *Eur. Phys. J. E* **35** 58

[3] Qiu X L and Tong P 2001 *Phys. Rev. E* **64** 036304

[4] Ashkenazi S and Steinberg V 1999 *Phys. Rev. Lett.* **83** 3641

[5] Verdoold J, Tummers M J and Hanjalic K 2006 *Phys. Rev. E* **73** 056304

[6] Xia K Q, Sun C and Zhou S Q 2003 *Phys. Rev. E* **68** 066303

[7] Liot O, Ehlinger Q, Rusaouën E, Coudarchet T, Salort J and Chillà F 2017 *Phys. Rev. Fluids* **2** 044605

[8] Verdoold J, Tummers M J and Hanjalić K 2009 *Phys. Rev. E* **80** 037301

[9] Valori V, Elsinga G, Rohde M, Tummers M, Westerweel J and van der Hagen T 2017 *Phys. Rev. E* **95** 053113

[10] Kästner C, Resagk C, Westphalen J, Junghähnel M, Cierpka C and Schumacher J 2018 *Exp. Fluids* **59**

[11] Valori V, Elsinga G, Rohde M, Westerweel J and van der Hagen T 2019 *Exp. Fluids* **60**

[12] Ni R, Huang S D and Xia K Q 2012 *J. Fluid Mech.* **692** 395–419

[13] Liot O, Gay A, Salort J, Bourgoin M and Chillà F 2016 *Phys. Rev. Fluids* **1** 064406

[14] Sano M, Wu X Z and Libchaber A 1989 *Phys. Rev. A* **40** 6421–6430

[15] Chavanne X, Chillà F, Castaing B, Hébral B, Chabaud B and Chaussy J 1997 *Phys. Rev. Lett.* **79** 3648–3651

[16] Niemela J J, Skrbek L, Sreenivasan K R and Donnelly R J 2001 *J. Fluid Mech.* **449** 169–178

[17] Musilová V, Králik T, Mantia M L, Macek M, Urban P and Skrbek L 2017 *J. Fluid Mech.* **832** 721–744

[18] Belkadi M, Guislain L, Sergent A, Podvin B, Chillà F and Salort J 2020 *J. Fluid Mech.* **895** A7

[19] Xie Y C and Xia K Q 2017 *J. Fluid Mech.* **825** 573–599

[20] Stevens R J A M, van der Poel E P, Grossmann S and Lohse D 2013 *J. Fluid Mech.* **730** 295–308

[21] He X, Funfschilling D, Bodenschatz E and Ahlers G 2012 *New J. Phys.* **14** 063030

[22] Chavanne X, Chillà F, Chabaud B, Castaing B and Hébral B 2001 *Phys. fluids* **13** 1300–1320

[23] Niemela J J and Sreenivasan K R 2003 *J. Fluid Mech.* **481** 355–384

[24] Niemela J and Sreenivasan K 2006 *J. Fluid Mech.* **557** 411–422

[25] Kraichnan R H 1962 *Phys. Fluids* **5** 1374–1389

[26] Gauthier F, Salort J, Bourgeois O, Garden J L, du Puits R, Thess A and Roche P E 2009 *EPL* **87** 44006

[27] Roche P E, Gauthier F, Kaiser R and Salort J 2010 *New J. Phys.* **12** 085014

[28] He X, van Gils D P M, Bodenschatz E and Ahlers G 2015 *New J. Phys.* **17** 063028

[29] Fincham A and Delerce G 2000 *Exp. Fluids Suppl.* **29** S13–S22

[30] Dubrulle B 2002 *Eur. Phys. J. B* **28** 361–367

[31] Wu X Z 1991 Ph.D. thesis University of Chicago

[32] Roche P E 2020 *New J. Phys.* **22** 073056

[33] Belkadi M, Sergent A, Fraigneau Y and Podvin B 2021 *J. Fluid Mech.* **923**

[34] Zhu X, Stevens R J A M, Verzicco R and Lohse D 2017 *Phys. Rev. Lett.* **119** 154501